

# We are IntechOpen, the world's leading publisher of Open Access books Built by scientists, for scientists

4,800

Open access books available

122,000

International authors and editors

135M

Downloads

Our authors are among the

154

Countries delivered to

TOP 1%

most cited scientists

12.2%

Contributors from top 500 universities



WEB OF SCIENCE™

Selection of our books indexed in the Book Citation Index  
in Web of Science™ Core Collection (BKCI)

Interested in publishing with us?  
Contact [book.department@intechopen.com](mailto:book.department@intechopen.com)

Numbers displayed above are based on latest data collected.  
For more information visit [www.intechopen.com](http://www.intechopen.com)



# Scattering from Multilayered Graphene-Based Cylindrical and Spherical Particles

*Shiva Hayati Raad, Zahra Atlasbaf and Mauro Cuevas*

## Abstract

This chapter discusses various approaches for calculating the modified Mie-Lorenz coefficients of the graphene-based multilayered cylindrical and spherical geometries. Initially, the Kubo model of graphene surface conductivity is discussed. Then, according to it, the formulations of scattering from graphene-based conformal particles are extracted. So, we have considered a graphene-wrapped cylinder and obtained its scattering coefficients by considering graphene surface currents on the shell. Later, a layered nanotube with multiple stacked graphene-dielectric interfaces is introduced, and for analyzing the plane wave scattering, graphene surface conductivity is incorporated in the transfer matrix method (TMM). Unlike the previous section, the dielectric model of graphene material is utilized, and the boundary conditions are applied on an arbitrary graphene interface, and a matrix-based formulation is concluded. Then, various examples ranging from super-scattering to super-cloaking are considered. For the scattering analysis of the multilayered spherical geometries, recurrence relations are introduced for the corresponding modified Mie-Lorenz coefficients by applying the boundary conditions at the interface of two adjacent layers. Later, for a sub-wavelength nanoparticle with spherical morphology, the full electrodynamics response is simplified in the electrostatic regime, and an equivalent circuit is proposed. Various practical examples are included to clarify the importance of scattering analysis for graphene-based layered spheres in order to prove their importance for developing novel optoelectronic devices.

**Keywords:** multilayered, graphene, spherical, cylindrical, nanoparticles, modified Mie-Lorenz theory, 2D material

## 1. Introduction

Cylindrically layered structures have various exotic applications. For instance, a metal-core dielectric-shell nano-wire has been proposed for the cloaking applications in the visible spectrum. The functionality of this structure is based on the induction of antiparallel currents in the core and shell regions, and the design procedure is the so-called scattering cancelation technique [1]. Experimental realization of a hybrid gold/silicon nanowire photodetector proves the practicality of these structures [2]. As an alternative approach for achieving an invisible cloak, cylindrically wrapped impedance surfaces are designed by a periodic arrangement of metallic patches, and the approach is denominated as mantle cloaking [3].

Conversely, cylindrically layered structures can be designed in a way that they exhibit a scattering cross-section far exceeding the single-channel limit. This phenomenon is known as super-scattering and has various applications in sensing, energy harvesting, bio-imaging, communication, and optical devices [4, 5]. Moreover, a cylindrical stack of alternating metals and dielectrics behaves as an anisotropic cavity and exhibits a dramatic drop of the scattering cross-section in the transition from hyperbolic to elliptic dispersion regimes [6, 7]. The Mie-Lorenz theory is a powerful, an exact, and a simple approach for designing and analyzing the aforementioned structures.

Multilayered spherical structures have also attracted lots of interests in the field of optical devices. A dielectric sphere made of a high index material supports electric and magnetic dipole resonances which results in peaks in the extinction cross-section [8]. Moreover, by covering the dielectric sphere with a plasmonic metal shell, an invisible cloak is realizable, which is useful for sensors and optical memories [9]. By stacking multiple metal-dielectric shells, an anisotropic medium for scattering shaping can be achieved [10].

From the above discussions, it can be deduced that tailoring the Mie-Lorenz resonances in the curved particles results in developing novel optical devices. In this chapter, we are going to extend the realization of various optical applications based on the excitations of localized surface plasmons (LSP) in graphene-wrapped cylindrical and spherical particles. To this end, initially we introduce a brief discussion of modeling graphene material based on corresponding surface conductivity or dielectric model. Later, we extract the modified Mie-Lorenz coefficients for some curved structures with graphene interfaces. The importance of developed formulas has been proven by providing various design examples. It is worth noting that graphene-wrapped particles with a different number of layers have been proposed previously as refractive index sensors, waveguides, super-scatterers, invisible cloaks, and absorbers [11–15]. Our formulation provides a unified approach for the plane wave and eigenmode analysis of graphene-based optical devices.

Graphene is a 2D carbon material in a honeycomb lattice that exhibits extraordinary electrical and mechanical properties. In order to solve Maxwell's equations in the presence of graphene, two approaches are applied by various authors, and we will review them in the following paragraphs. It should be noted that although we are discussing the graphene planar model, we will use the same formulas for the curved geometries when the number of carbon atoms exceeds  $10^4$ , letting us neglect the effect of defects. Therefore, the radii of all cylinders and spheres are considered to be greater than 5 nm [16]. Moreover, bending the graphene does not have any considerable impact on the properties of its surface plasmons, except for a small downshift of the frequency. **Figure 1** shows the propagation of the graphene surface plasmons on the S-shaped and G-shaped curves [17].

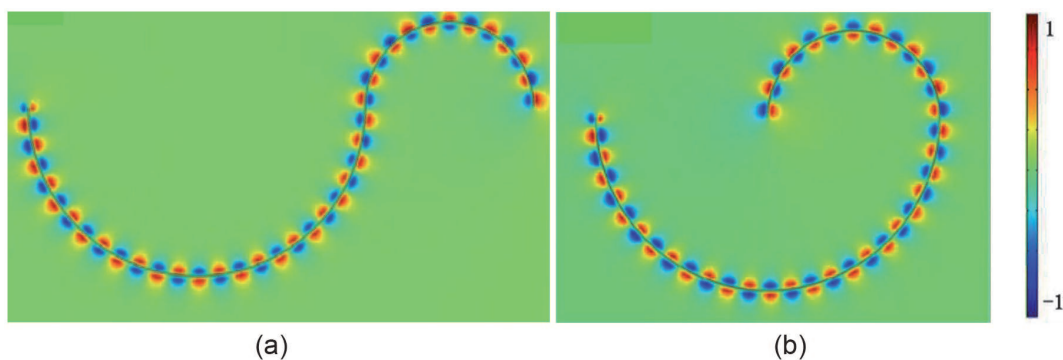


**Figure 1.**

*Propagation of graphene surface plasmons on curved structures: (a) S-shaped and (b) G-shaped [17].*

Since graphene material is atomically thin, in order to consider its impact on the electromagnetic response of a given structure, boundary conditions at the interface can be simply altered. To this end, graphene surface currents that are proportional to its surface conductivity should be accounted for ensuring the discontinuity of tangential magnetic fields. In the infrared range and below, we can describe the graphene layer with a complex-valued surface conductivity  $\sigma$  which may be modeled using the Kubo formulas [18, 19]. The intraband and interband contributions of graphene surface conductivity under local random phase approximations read as [18]:

$$\sigma_{\text{intra}}(\omega) = \frac{2ie^2k_B T}{\pi\hbar^2(\omega + i\Gamma)} \ln \left[ 2 \cosh \left( \frac{\mu_c}{2k_B T} \right) \right] \quad (1)$$

$$\sigma_{\text{inter}} \approx \frac{e^2}{4\hbar} \left[ \frac{1}{2} + \frac{1}{\pi} \arctan \left( \frac{\hbar\omega - 2\mu_c}{2k_B T} \right) - \frac{i}{2\pi} \ln \frac{(\hbar\omega + 2\mu_c)^2}{(\hbar\omega - 2\mu_c)^2 + (2k_B T)^2} \right] \quad (2)$$

The parameters  $\hbar$ ,  $e$ ,  $\mu_c$ ,  $\Gamma$ , and  $T$  are reduced Plank's constant, electron charge, chemical potential, charge carriers scattering rate, and temperature, respectively. The above equations are valid for the positive valued chemical potentials. Moreover, graphene-based structures can be analyzed by assigning a small thickness of  $\Delta \approx 0.35 \text{ nm}$  to the graphene interface and later approaching it to the zero. In this method, by defining the volumetric conductivity as  $\sigma_{g,V} = \sigma_g/\Delta$  and using it in

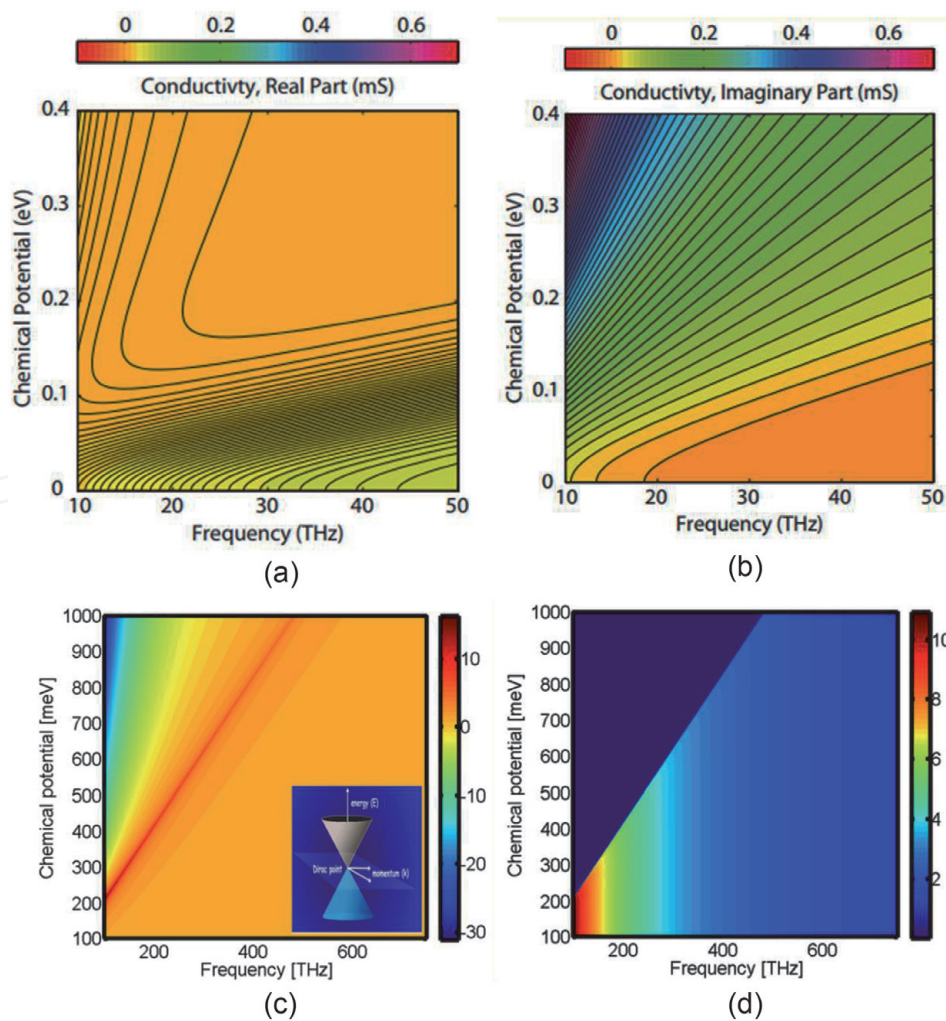


**Figure 2.** (a) and (b) the real and imaginary parts of graphene surface conductivity [20] and (c) and (d) the real and imaginary parts of graphene equivalent permittivity [21].

Maxwell's curl equations, the equivalent complex permittivity of the layer can be obtained as [20]:

$$\varepsilon_{g,eq} = \left( -\frac{\sigma_{g,i}}{\omega\Delta} + \varepsilon_0 \right) + i \left( \frac{\sigma_{g,r}}{\omega\Delta} \right) \quad (3)$$

where subscripts  $r$  and  $i$  represent the real and imaginary parts of the surface conductivity, respectively. Both models will be used in the following sections.

**Figure 2(a)** and **(b)** shows the real and imaginary parts of graphene surface conductivity at the temperature of  $T = 300^\circ\text{K}$ . The real part of the conductivity accounts for the losses, while the positive valued imaginary parts represent the plasmonic properties [20]. Moreover, the real and imaginary parts of the graphene equivalent bulk permittivity are shown in **Figure 2(c)** and **(d)**. The negative valued real relative permittivity represents the plasmonic excitation, and the imaginary part of the permittivity represents the losses [21]. It should be noted that all of the formulas of this chapter are adapted with  $\exp(-i\omega t)$  time-harmonic dependency.

## 2. Graphene-coated cylindrical tubes

In this section, the modified Mie-Lorenz coefficients of a single-layered graphene-coated cylindrical tube will be extracted. The formulation is expanded into the multilayered graphene-based tubes through exploiting the TMM method, and later, various applications of the analyzed structures, including emission and radiation properties, complex frequencies, super-scattering, and super-cloaking, will be explained.

### 2.1 Scattering from graphene-coated wires

Let us consider a graphene-wrapped infinitely long cylindrical tube. The structure is shown in **Figure 3(a)**, and it is considered that a  $\text{TE}^z$ -polarized plane wave illuminates the cylinder. In general, TE and TM waves are coupled in the cylindrical geometries. For the normally incident plane waves, they become decoupled, and they can be treated separately. For simplicity, we consider the normal incidence of plane waves where the wave vector  $k$  is perpendicular to the cylinder axis.

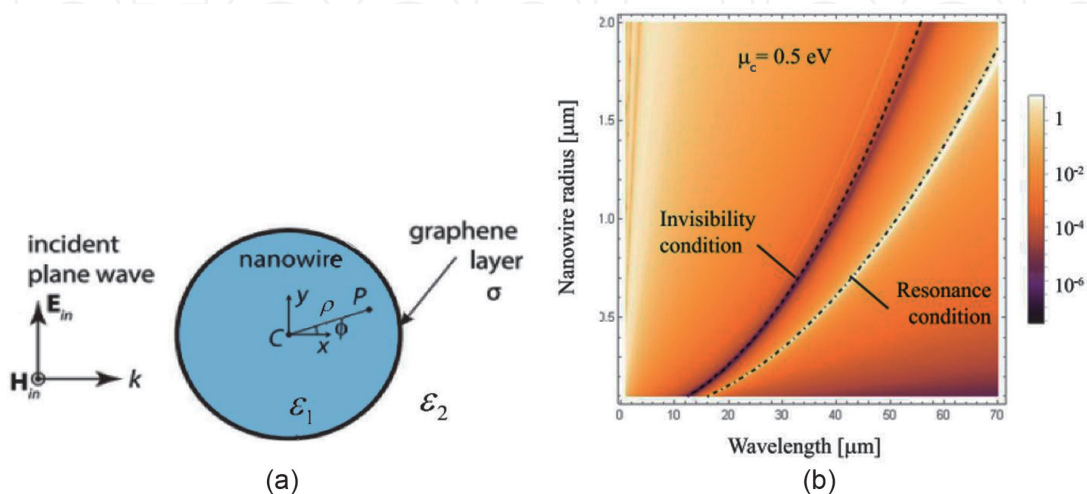


**Figure 3.**

(a) A single-layered graphene-coated cylinder under  $\text{TE}^z$  plane wave illumination and (b) corresponding scattering efficiency for  $\varepsilon_1 = 3.9$  and  $\mu_c = 0.5$  eV. The normalization factor in this figure is the diameter of the cylinder [23].

In order to obtain the modified Mie-Lorenz coefficients, the incident, scattered, and internal electromagnetic fields are expanded in terms of cylindrical coordinates special functions which are, respectively, the Bessel functions and exponentials in the radial and azimuthal directions. In order to exploit a terse mathematical notation, the vector wave functions are introduced as [22]:

$$\mathbf{M}_n = k \left( in \frac{Z_n(k\rho)}{k\rho} \hat{\rho} - Z'_n(k\rho) \hat{\phi} \right) e^{in\phi} \quad (4)$$

$$\mathbf{N}_n = k Z_n(k\rho) e^{in\phi} \hat{z} \quad (5)$$

The complete explanation of the above vector wave functions and their self and mutual orthogonally relations can be found in the classic electromagnetic books [22]. In the above equation,  $Z_n$  is the solution of the Bessel differential equation, and  $n$  is its order. It is clear that in the environment, the radial field contains the Hankel function of the first kind in order to account for the radiation condition at infinity, while in the medium region, the Bessel function is utilized to satisfy the finiteness condition at the origin of the structure.

In the graphene-based cylindrical structures, the plasmonic state is achieved via illuminating a TE<sup>z</sup> wave to the structure. Therefore, for the normal illumination, the incident, scattered, and dielectric electromagnetic fields are shown with the superscripts  $l = in, sca, d$ , respectively, and they read as [23]:

$$\mathbf{H}_l = \frac{H_0}{k_l} \sum_{n=-\infty}^{\infty} A_n i^n \mathbf{N}_n(k_l \rho) \quad (6)$$

$$\mathbf{E}_l = \frac{E_0}{k_l} \sum_{n=-\infty}^{\infty} B_n i^n \mathbf{M}_n(k_l \rho) \quad (7)$$

where  $H_0$  and  $E_0$  are the magnitudes of the incident electric and magnetic fields, respectively, and they are related via the intrinsic impedance of the free space. The wavenumber in the region  $l$  is denoted by  $k_l$ . The coefficients  $[A_n, B_n]$  are, respectively,  $[1, 1]$ ,  $[a_n, b_n]$ , and  $[c_n, d_n]$  for the incident, scattered, and core regions. Moreover,  $a_n$  and  $b_n$  are the well-known Mie-Lorenz coefficients, which are called the modified Mie-Lorenz coefficients for the scattering analysis of graphene-based structures.

The boundary conditions at the graphene interface at  $\rho = R_1$  are the continuity of the tangential electric fields along with the discontinuity of tangential magnetic fields. Therefore:

$$\hat{\phi} \cdot \mathbf{E}_d = \hat{\phi} \cdot (\mathbf{E}_{sca} + \mathbf{E}_{in}) \quad (8)$$

$$\hat{z} \cdot \mathbf{H}_d = \hat{z} \cdot (\mathbf{H}_{sca} + \mathbf{H}_{in}) + \hat{\phi} \cdot \mathbf{E}_d \sigma \quad (9)$$

By applying the boundary conditions in the expanded fields, the linear system of equations for extracting the unknowns can be readily obtained. The solution of the extracted equations for the scattering coefficients leads to:

$$a_n = \frac{k_1 J'_n(k_1 R_1) \left[ \varepsilon_2 J_n(k_2 R_1) - i \frac{k_2 \sigma}{\omega \varepsilon_0} J'_n(k_2 R_1) \right] - k_2 \varepsilon_1 J_n(k_1 R_1) J'_n(k_2 R_1)}{k_2 H_n^{(1)'}(k_2 R_1) \left[ \varepsilon_1 J_n(k_1 R_1) + i \frac{k_1 \sigma}{\omega \varepsilon_0} J'_n(k_1 R_1) \right] - k_1 \varepsilon_2 H_n^{(1)}(k_2 R_1) J'_n(k_1 R_1)} \quad (10)$$

$$b_n = \frac{k_2 \varepsilon_1 \left[ H_n^{(1)'}(k_2 R_1) J_n(k_2 R_1) - H_n^{(1)}(k_2 R_1) J'_n(k_2 R_1) \right]}{k_2 H_n^{(1)'}(k_2 R_1) \left[ \varepsilon_1 J_n(k_1 R_1) + i \frac{k_1 \sigma}{\omega \varepsilon_0} J'_n(k_1 R_1) \right] - k_1 \varepsilon_2 H_n^{(1)}(k_2 R_1) J'_n(k_1 R_1)} \quad (11)$$

The same procedure can be repeated for the  $\text{TM}^z$  illumination. The normalized scattering cross-section (NSCS) reads as:

$$\text{NSCS} = \sum_{n=-\infty}^{\infty} |a_n|^2 \quad (12)$$

where the normalization factor is the single-channel scattering limit of the cylindrical structures. In order to have some insight into the scattering performance of graphene-wrapped wires, the scattering efficiency for  $\epsilon_1 = 3.9$  and  $\mu_c = 0.5$  eV is plotted in **Figure 3(b)** by varying the radius of the wire. As the figure illustrates, a peak valley line shape occurs in each wavelength. They correspond to invisibility and scattering states and will be further manipulated in the next sections to develop some novel devices. The excitation frequency of the plasmons is the complex poles of the extracted coefficients [24] which will be discussed in the next subsection. Interestingly, the scattering states of graphene-coated dielectric cores are polarization-dependent. By using a left-handed metamaterial as a core, this limitation can be obviated [25].

### 2.1.1 Eigenmode problem and complex frequencies

As in any resonant problem, additional information can be obtained by studying the solutions to the boundary value problem in the absence of external sources (eigenmode approach). Although, from a formal point of view, this approach has many similar aspects with those developed in previous sections, the eigenmode problem presents an additional difficulty related to the analytic continuation in the complex plane of certain physical quantities. Due to the fact that the electromagnetic energy is thus leaving the LSP (either by ohmic losses or by radiation towards environment medium), the LSP should be described by a complex frequency where the imaginary part takes into account the finite lifetime of such LSP. The eigenmode approach is not new in physics, but its appearance is associated to any resonance process (at an elementary level could be an RLC circuit), where the complex frequency is a pole of the analytical continuation to the complex plane of the response function of the system (e.g., the current on the circuit). Similarly, in the eigenmode approach presented here, the complex frequencies correspond to poles of the analytical continuation of the multipole terms (Mie-Lorenz coefficients) in the electromagnetic field expansion.

In order to derive complex frequencies of LSP modes in terms of the geometrical and constitutive parameters of the structure, we use an accurate electrodynamic formalism which closely follows the usual separation of variable approach developed in Section 2.1. We can obtain a set of two homogeneous equations for the  $m$ -th LSP mode [26]:

$$\begin{aligned} \frac{k_2}{\epsilon_2} H_n^{(1)'}(x_2) a_n - \frac{k_1}{\epsilon_1} J_n'(x_1) b_n &= 0 \\ H_n^{(1)}(x_2) a_n - J_n(x_1) b_n &= \frac{\sigma k_1}{\omega \epsilon_0 \epsilon_1} b_n J_n'(x_1) \end{aligned} \quad (13)$$

where the prime denotes the first derivative with respect to the argument of the function and  $x_j = k_j R_1$  ( $j = 1, 2$ ). For this system to have a nontrivial solution, its determinant must be equal to zero, a condition which can be written as:

$$D_n = h_n(x_2) - j_n(x_1) + \sigma \omega i R_1 j_n(x_1) h_n(x_2) = 0 \quad (14)$$

where  $j_n(x) = \frac{J'_n(x)}{xJ_n(x)}$ ,  $h_n(x) = \frac{H_n^{(1)'}(x)}{xH_n^{(1)}(x)}$ . This condition is the dispersion relation of LSPs, and it determines the complex frequencies in terms of all the parameters of the wire cylinder.

### 2.1.2 Non-retarded dispersion relation

When the size of the cylinder is small compared to the eigenmode wavelength, i.e.,  $\lambda_n = \frac{2\pi c}{\omega_n} \gg R_1$ , where  $c$  is the speed of light in free space, Eq. (13) can be approximated by using the quasistatic approximation as follows. Using the small argument asymptotic expansions for Bessel and Hankel functions, the functions  $j_n(x) \approx \frac{n}{x^2}$  and  $h_n(x) \approx -\frac{n}{x^2}$  [27]. Thus, the dispersion relation (14) adopts the form:

$$i\omega\varepsilon_0 \frac{\varepsilon_1 + \varepsilon_2}{\sigma} = \frac{n}{R_1} \quad (15)$$

Taking into account that in the non-retarded regime the propagation constant of the plasmon propagating along perfectly flat graphene sheet can be approximated by:

$$k_{sp} = i\omega\varepsilon_0 \frac{\varepsilon_1 + \varepsilon_2}{\sigma}, \quad (16)$$

it follows that the dispersion relation (14) for LSPs in dielectric cylinders wrapped with a graphene sheet can be written as:

$$k_{sp}2\pi R_1 = 2\pi n \quad (17)$$

where  $n$  is the LSP multipole order. The dispersion Eq. (17), known as Bohr condition, states that the  $n$ -th LSP mode of a graphene-coated cylinder accommodates along the cylinder perimeter exactly  $n$  oscillation periods of the propagating surface plasmon corresponding to the flat graphene sheet.

For large doping ( $\mu_c \gg k_B T$ ) and relatively low frequencies ( $\hbar\omega \ll \mu_c$ ), the intraband contribution to the surface conductivity (1), the Drude term, plays the leading role. In this case, the non-retarded dispersion equation Eq. (14) is written as:

$$\varepsilon_1 + \varepsilon_2 = \frac{e^2 \mu_c n}{\hbar^2 \pi \varepsilon_0 R_1 \omega (\omega + i\gamma_c)} \quad (18)$$

which can be analytically solved for the plasmon eigenfrequencies,

$$\omega_n = \sqrt{\frac{\omega_0^2 n^2}{\varepsilon_1 + \varepsilon_2} - \left(\frac{\gamma_c}{2}\right)^2} - i\frac{\gamma_c}{2} \approx \frac{n\omega_0}{\sqrt{\varepsilon_1 + \varepsilon_2}} - i\frac{\gamma_c}{2}, \quad (19)$$

where  $\omega_0^2 = \frac{e^2 \mu_c}{\pi \varepsilon_0 \hbar^2 R_1}$  is the effective plasma frequency of the graphene coating. It is worth noting that the real part of  $\omega_n$  is proportional to  $\sqrt{\mu_c}$ , and as a consequence, the net effect of the chemical potential increment is to increase the spectral position of the resonance peaks when the structure is excited with a plane wave or a dipole emitter [28, 29].

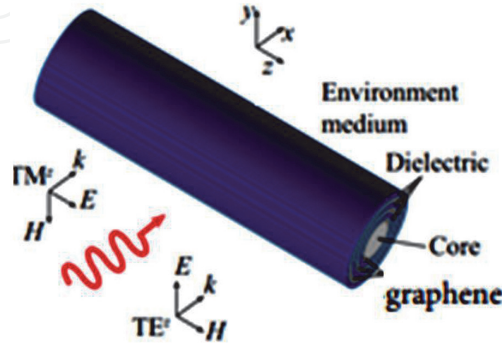
In the following example, we consider a graphene-coated wire with a core radius  $R_1 = 30$  nm, made of a non-magnetic dielectric material of permittivity  $\varepsilon_1 = 2.13$



$n$	FR ( $\mu\text{m}^{-1}$ )	AA ( $\mu\text{m}^{-1}$ )
1	$0.8868268 - i0.4105015 \times 10^{-3}$	$0.8873162 - i0.2532113 \times 10^{-3}$
2	$1.254676 - i0.2532181 \times 10^{-3}$	$1.254855 - i0.2532113 \times 10^{-3}$
3	$1.536735 - i0.2531644 \times 10^{-3}$	$1.536877 - i0.2532113 \times 10^{-3}$
4	$1.774508 - i0.2531757 \times 10^{-3}$	$1.774632 - i0.2532113 \times 10^{-3}$

**Table 1.**

Resonance frequencies  $\omega_n$  for the first four eigenmodes ( $1 \leq n \leq 4$ ),  $R_1 = 30 \text{ nm}$ ,  $\mu_c = 0.5 \text{ eV}$ ,  $\gamma_c = 0.1 \text{ meV}$ ,  $\epsilon_1 = 2.13$ ,  $\mu_1 = 1$ ,  $\epsilon_2 = 1$ , and  $\mu_2 = 1$  [26].


**Figure 4.**

Multilayered cylindrical structure consisting of alternating graphene-dielectric stacks under plane wave illumination. The 2D graphene shells are represented volumetrically for the sake of illustration [31].

immersed in the vacuum. The graphene parameters are  $\mu_c = 0.5 \text{ eV}$ ,  $\gamma_c = 0.1 \text{ meV}$ , and  $T = 300^\circ \text{ K}$ . **Table 1** shows the first four eigenfrequencies calculated by solving the full retarded (FR) dispersion Eq. (14) (second column) and by using the analytical approximation (AA) given by Eq. (19) (third column). Since the radius of the wire is small compared with the eigenmode wavelengths, good agreement is obtained between the complex FR and AA  $\omega_n$  values, even when the AA assigns  $\text{Im } \omega_n = -\gamma_c/2 \approx 0.25 \times 10^{-3} \mu\text{m}^{-1}$  to all multipolar plasmon modes.

## 2.2 Multilayered graphene-based cylindrical structures

In this section, multilayered cylindrical tubes with multiple graphene interfaces are of interest. In order to ease the derivation of the unknown expansion coefficients, matrix-based TMM formulation is generalized to the tubes with several graphene interfaces. Initially, consider a layered cylinder constructed by the staked ordinary materials under  $\text{TE}^z$  plane wave illumination, as shown in **Figure 4**. The total magnetic field at the environment can be expressed as the superposition of incident and scattered waves as in Section 2.1. The unknown expansion coefficients of the scattered wave can be determined by means of the  $T_n$  matrix defined as [30]:

$$T_n = [D_{n,C}(R_1)]^{-1} \cdot \left\{ \prod_{q=1}^N D_{n,q}(R_q) \cdot [D_{n,q}(R_{q+1})]^{-1} \right\} \cdot D_{n,N+1}(R_{q+1}) \quad (20)$$

where  $C$  represents the core layer. In the above equation, the dynamical matrix  $D_{n,q}$  of each region is constructed based on its constitutive and geometrical parameters distinguished through the subscript  $q$  ( $q = 1, 2, \dots, N$ ). We have:

$$D_{n,q}(x) = \begin{bmatrix} J_n(x_1) & Y_n(x_1) \\ z_q^{-1} J'_n(x_1) & z_q^{-1} Y'_n(x_1) \end{bmatrix} \quad (21)$$

The argument of the above special functions is  $x_1 = k_q x$ , and the TE<sup>z</sup> wave impedance equals  $z_q^{-1} = \sqrt{\epsilon_q}$ . After generating  $T_n$  matrix for the structure,  $a_n$  coefficients can be calculated as:

$$a_n = \frac{T_{n,21}}{T_{n,21} + iT_{n,22}} \quad (22)$$

In order to incorporate the graphene surface conductivity in the above formulas, let us consider each graphene interface as a thin dielectric with the equivalent complex permittivity defined in Eq. (3) and utilize the TMM formulation in the limiting case of a small radius at the graphene interface with the wave number of  $k_g$ , i.e.,  $R_{q+1} - R_q = t_g$ . At each boundary, using the Taylor expansion as  $J_n(k_g R_q) = J_n(k_g R_{q+1}) - t_g k_g J'_n(k_g R_{q+1})$  in the  $T_n$  matrix, the graphene interface can be represented by the following matrices. We have:

$$T_g^{TE} = \begin{bmatrix} 1 & -i\sigma\eta_0 \\ 0 & 1 \end{bmatrix} \quad (23)$$

$$T_g^{TM} = \begin{bmatrix} 1 & 0 \\ i\sigma\eta_0 & 1 \end{bmatrix} \quad (24)$$

where the free-space impedance  $\eta_0$  equals 377 ohms. Once  $T_n$  matrix is generated, the modified Mie-Lorenz coefficients and thus scattering cross-section are readily attainable. In the following subsections, the above equations will be used to design some novel optoelectronic devices.

### 2.2.1 Application in mantle cloaking

Widely tunable scattering cancelation is feasible by using patterned graphene-based patch meta-surface around the dielectric cylinder as shown in **Figure 5**. The surface impedance of the graphene patches can be simply and accurately calculated by closed-form formulas, to be inserted in the modified Mie-Lorenz theory [32].

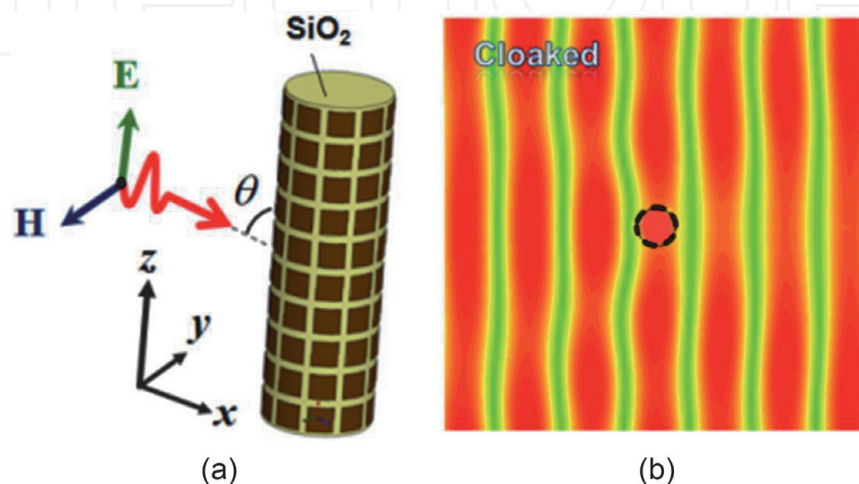


**Figure 5.**  
 (a) Electromagnetic cloaking of a dielectric cylinder using graphene meta-surface and (b) corresponding electric field distribution [32].

## 2.2.2 Application in super-scattering

Let us consider a triple shell graphene-based nanotube under plane wave illumination, as shown in **Figure 6(a)**. This structure is used to design a dual-band super-scatterer in the infrared frequencies. To this end, modified Mie-Lorenz coefficients of various scattering channels should have coincided with the proper choice of geometrical and optical parameters. In order to construct the  $T_n$  matrix for this geometry, one needs to multiply nine  $2 \times 2$  dynamical matrices, which is mathematically complex for analytical scattering manipulation. Therefore, the associated planar structure, shown in **Figure 6(b)**, is used to develop the dispersion engineering method as a quantitative design procedure of the super-scatter. The separations of the free-standing graphene layers are  $d_1 = d_2 = 45$  nm in the planar structure, and the transmission line model is used to analyze it. Moreover, the chemical potential of lossless graphene material is  $\mu_c = 0.2$  eV in all layers. The dispersion diagram of the planar structure is illustrated in **Figure 7(a)**, which predicts the presence of three plasmonic resonances in each scattering channel of the tube at around the frequencies that fulfill  $\beta R_{\text{eff}} = n$ , where  $R_{\text{eff}}$  is the mean of the radii of all layers and  $\beta$  is the propagation constant of the plasmons in the planar structure. This condition is known as Bohr's quantization formula [30], and its validity for our specific structure is proven by means of the previously developed formulas in **Figure 7(b)**. Eqs. (12), (22), and (23) are used to obtain this figure.

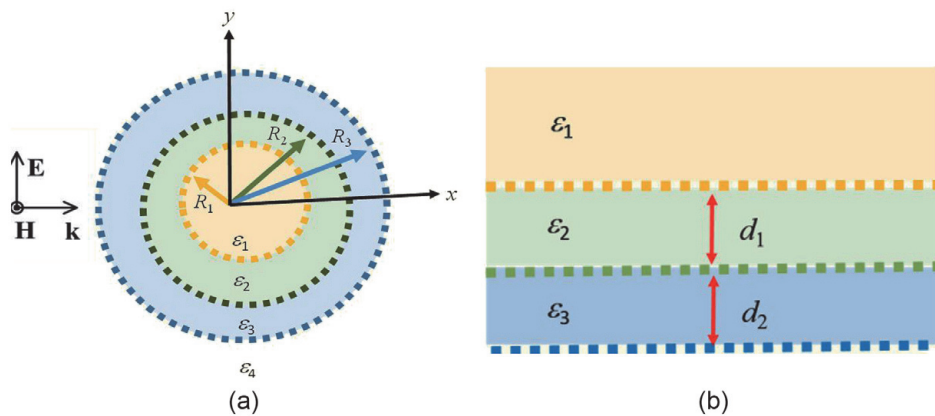


**Figure 6.** (a) Multilayered cylindrical nanotube with three graphene shells and (b) associated planar structure [30].  $R_1$  is denoted with  $R_c$  in the text.

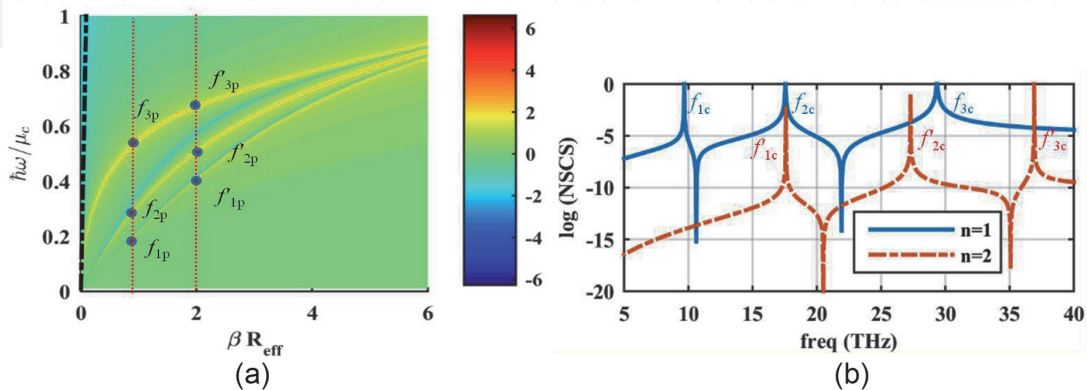


**Figure 7.** (a) Dipole and quadrupole Mie-Lorenz scattering coefficients for the tube of **Figure 6** and (b) dispersion diagram of the associated planar structure [30].  $f_{1p}$ ,  $f_{2p}$ , and  $f_{3p}$  are the plasmonic resonances of the dipole mode predicted by the planar configuration. The prime denotes the same information for the quadrupole mode.  $f_{1e}$ ,  $f_{2e}$ , and  $f_{3e}$  are the same information calculated by the exact modified Mie-Lorenz theory of the multilayered cylindrical structure.

In order to design a dual-band super-scatterer, the plasmonic resonances of two scattering channels have coincided by fine-tuning the results of the Bohr's model. The optimized geometrical and constitutive parameters are  $R_c = 45.45$  nm,  $d_1 = 45.05$  nm,  $d_2 = 43.23$  nm,  $\epsilon_1 = 3.2$ ,  $\epsilon_2 = 2.1$ ,  $\epsilon_3 = 2.2$ , and  $\epsilon_4 = 1$ . **Figure 8** shows the NSCS and magnetic field distribution for the dual operating bands of the structure. It is clear that NSCS exceeds the single-channel limit by the factor of 4, and in the corresponding magnetic field, there is a large shadow around the nanometer-sized cylinder at each operating frequency. Other designs are also feasible by altering optical and geometrical parameters. Furthermore, the far-field radiation pattern is a hybrid dipole-quadrupole due to simultaneous excitation of the first two channels. It should be noted that an inherent characteristic of the super-scatterer design using plasmonic graphene material is extreme sensitivity to the parameters. Moreover, in the presence of losses, the scattering amplitudes do not reach the single-channel limit anymore, and this restricts the practical applicability of the concepts to low-frequency windows.

### 2.2.3 Application in simultaneous super-scattering and super-cloaking

As another example, the dispersion diagram of **Figure 7(a)** along with Foster's theorem has been used to conclude that each scattering channel of the triple shell tube contains two zeros which are lying between the plasmonic resonances, predicted by the Bohr's model. Later, we have coincided the zeros and poles of the first two scattering channels in order to observe super-scattering and super-cloaking simultaneously [33]. The optimized material and geometrical parameters are  $\epsilon_c = 3.2$ ,  $\epsilon_1 = \epsilon_2 = 2.1$ ,  $R_c = 45.45$  nm,  $d_1 = 46.25$  nm, and  $d_2 = 46.049$  nm. The NSCS curves corresponding to the super-cloaking and super-scattering regimes are illustrated in

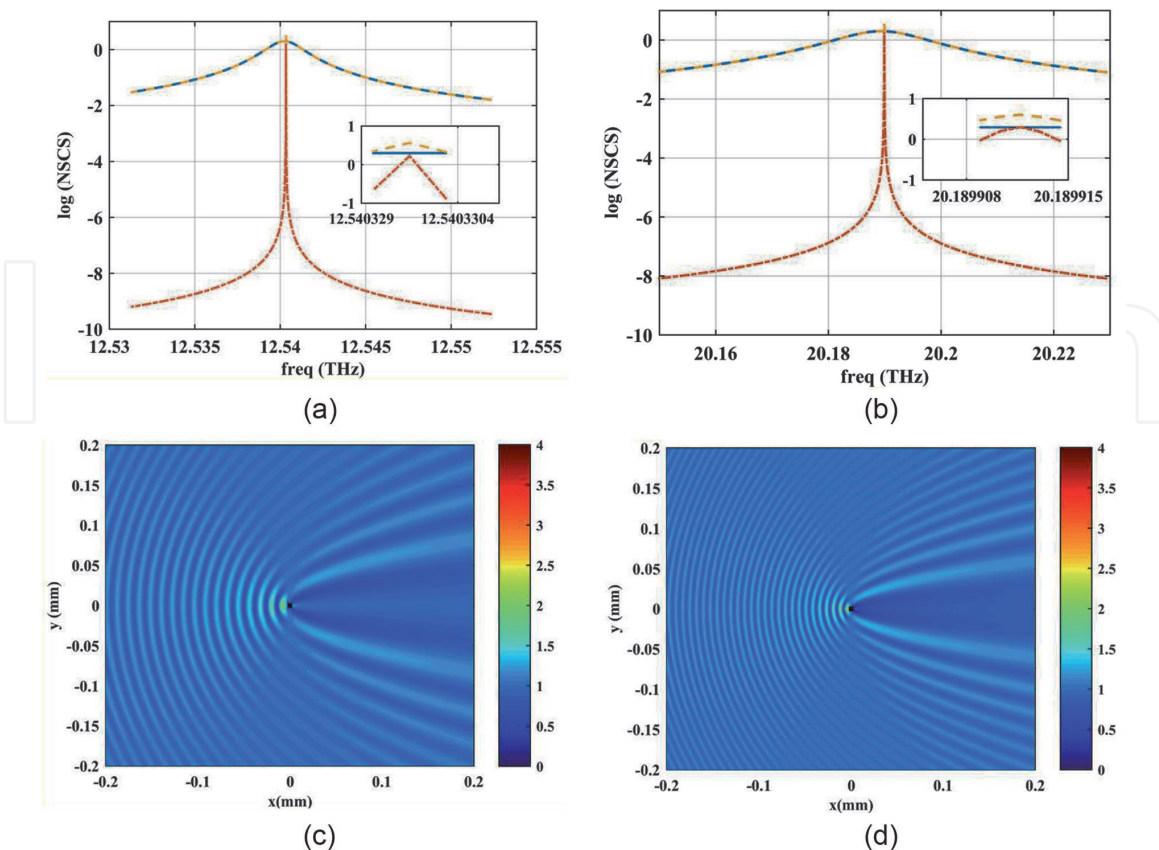


**Figure 8.** (a) and (b) The NSCS of dual-band super-scatterer respectively, in the first and second operating frequencies and (c) and (d) corresponding magnetic field distributions [30].

**Figure 9(a)** and **(b)**, as well as the expected phenomenon, is clearly observed. The corresponding magnetic field distributions, shown in **Figure 9(c)** and **(d)**, also manifest the reduced and enhanced scatterings in the corresponding operating bands, respectively. Similar to the dual-band super-scatterer of the previous section, the performance of this structure is very sensitive to the optical, material, and geometrical parameters. By further increasing the number of graphene shells, other plasmonic resonances and zeros can be achieved for the manipulation of the optical response.

### 3. Graphene-coated spherical structures

In this section, multilayered graphene-coated particles with spherical morphology are investigated, and corresponding modified Mie-Lorenz coefficients are extracted by expanding the incident, scattered, and transmitted electromagnetic fields in terms of spherical harmonics. It is clear that by increasing the number of graphene layers, further degrees of freedom for manipulating the optical response can be achieved. For the simplicity of the performance optimization, an equivalent RLC circuit is proposed in the quasistatic regime for the sub-wavelength plasmons, and various practical examples are presented.

#### 3.1 Multilayered graphene-based spherical structures

In this section, the most general graphene-based structure with  $N$  dielectric layers, as shown in **Figure 10**, is considered, and plane wave scattering is analyzed through extracting recurrence relations for modified Mie-Lorenz coefficients. It should be noted that since, in the TMM method, multiple matrix inversions are

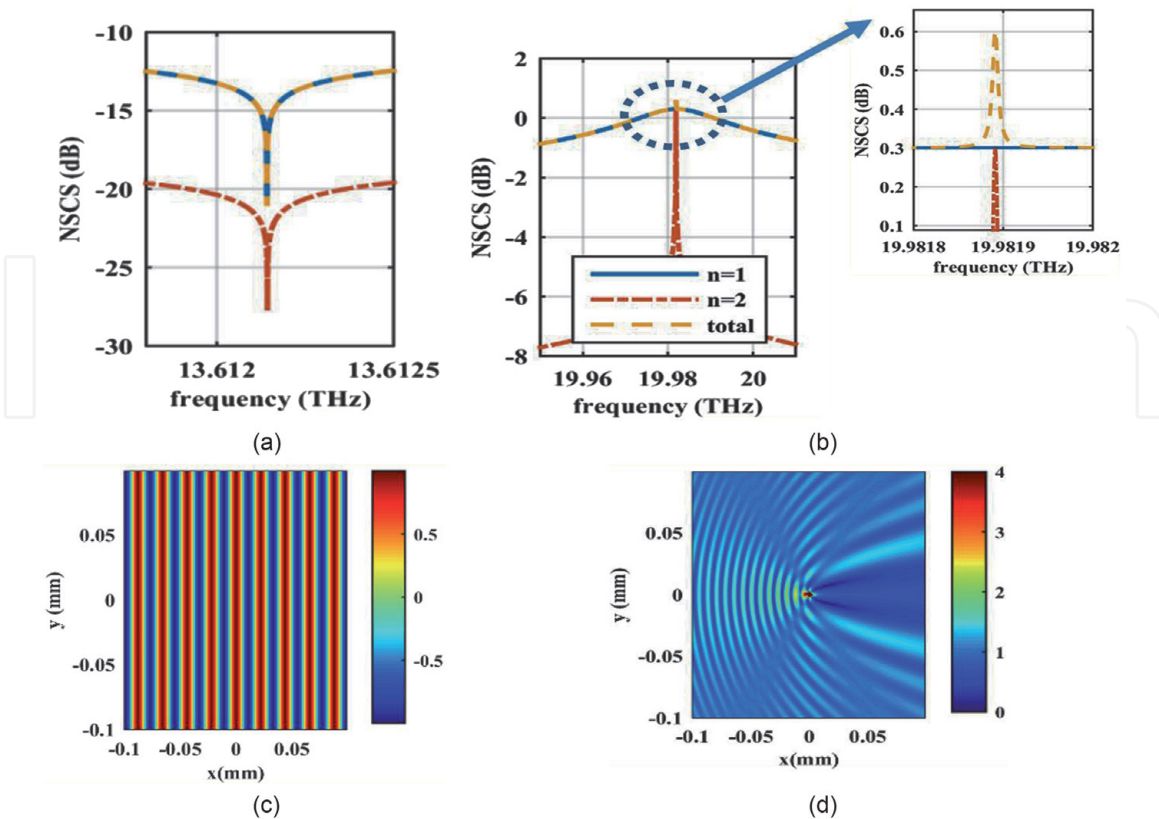


**Figure 9.** Simultaneous super-scattering and super-cloaking using the structure of **Figure 6**. NSCS for (a) super-cloaking and (b) super-scattering regimes and corresponding magnetic field distributions, respectively, in (c) and (d) [33].

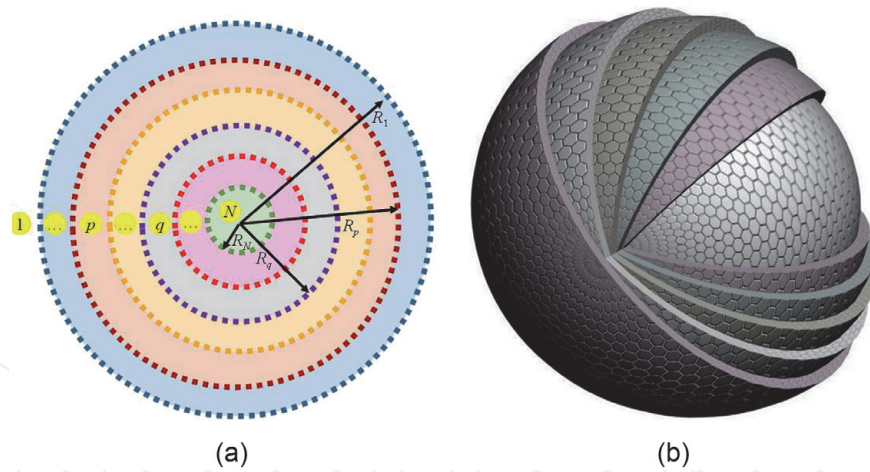


**Figure 10.** Spherical graphene-dielectric stack (a) 2D and (b) 3D views [34]. Please note that the numbering of the layers is started from the outermost layer in order to preserve the consistency with the reference paper [35].

necessary, unlike the cylindrically layered structures of the previous section, the spherical geometries are analyzed through recurrence relations. Also, scattering from a single graphene-coated sphere has been formulated elsewhere [16], and it can be simply attained as the special case of our formulation.

The scattering analysis is very similar to that of the single-shell sphere [16], unless the Kronecker delta function is used in the expansions in order to find the electromagnetic fields of any desired layer with terse expansions. Therefore [34]:

$$\mathbf{E}_i = E_0 \sum_n \sum_m i^n \frac{2n+1}{n(n+1)} \left\{ \mathbf{M}_{mn}^{(1)} - i\mathbf{N}_{mn}^{(1)} \right\} \quad (25)$$

$$\begin{aligned} \mathbf{E}_{scat}^p = E_0 \sum_n \sum_m i^n \frac{2n+1}{n(n+1)} \times \\ \left\{ \left(1 - \delta_p^N\right) B_{H}^p \mathbf{M}_{mn}^{(1)} - i \left(1 - \delta_p^N\right) B_{V}^p \mathbf{N}_{mn}^{(1)} + \left(1 - \delta_p^1\right) D_{H}^p \mathbf{M}_{mn} - i \left(1 - \delta_p^1\right) D_{V}^p \mathbf{N}_{mn} \right\} \end{aligned} \quad (26)$$

By considering  $z_n$  as either  $j_n$  or  $h_n^{(1)}$ , which stand for the spherical Bessel and Hankel functions of the first kind with order  $n$ , respectively, and  $P_n^m$  as the associated Legendre function of order  $(n, m)$ , the vector wave functions are defined as follows:

$$\mathbf{M}_{mn}(k_p) = z_n(k_p r) e^{im\phi} \left[ \frac{im}{\sin\theta} P_n^m(\cos\theta) \hat{\theta} - \frac{dP_n^m(\cos\theta)}{d\theta} \hat{\phi} \right] \quad (27)$$

$$\begin{aligned} \mathbf{N}_{mn}(k_p) = \frac{n(n+1)}{k_p r} z_n(k_p r) P_n^m(\cos\theta) e^{im\phi} \hat{r} + \\ \frac{1}{k_p r} \frac{d[rz_n(k_p r)]}{dr} \left[ \frac{dP_n^m(\cos\theta)}{d\theta} \hat{\theta} + \frac{im}{\sin\theta} P_n^m(\cos\theta) \hat{\phi} \right] e^{im\phi} \end{aligned} \quad (28)$$

where super-indices (1) in the vector wave functions show that the Hankel functions are used in the field expansions. The boundary conditions at the interface of adjacent layers read as:

$$\hat{r} \times \mathbf{E}^{(p)} = \hat{r} \times \mathbf{E}^{(p+1)} \quad (29)$$

$$\frac{1}{i\omega\mu_{p+1}} \hat{r} \times \nabla \times \mathbf{E}^{(p+1)} - \frac{1}{i\omega\mu_p} \hat{r} \times \nabla \times \mathbf{E}^{(p)} = \sigma_{(p+1)p} \hat{r} \times \left( \hat{r} \times \mathbf{E}^{(p)} \right) \quad (30)$$

Therefore, the linear system of equations resulting from the above conditions is:

$$\begin{bmatrix} \xi_n^{pp} B_H^p \\ \partial \xi_n^{pp} B_V^p \end{bmatrix} + \begin{bmatrix} \psi_n^{pp} (D_H^p + \delta_p^1) \\ \partial \psi_n^{pp} (D_V^p + \delta_p^1) \end{bmatrix} = \begin{bmatrix} \xi_n^{(p+1)p} B_H^{(p+1)} \\ \partial \xi_n^{(p+1)p} B_V^{(p+1)} \end{bmatrix} + \begin{bmatrix} \psi_n^{(p+1)p} D_H^{(p+1)} \\ \partial \psi_n^{(p+1)p} D_V^{(p+1)} \end{bmatrix} \quad (31)$$

$$\begin{aligned} & \frac{k_{p+1}}{\mu_{p+1}} \left( \begin{bmatrix} \partial \xi_n^{(p+1)p} B_H^{(p+1)} \\ \xi_n^{(p+1)p} B_V^{(p+1)} \end{bmatrix} + \begin{bmatrix} \partial \psi_n^{(p+1)p} D_H^{(p+1)} \\ \psi_n^{(p+1)p} D_V^{(p+1)} \end{bmatrix} \right) - \frac{k_p}{\mu_p} \left( \begin{bmatrix} \partial \xi_n^{pp} B_H^p \\ \xi_n^{pp} B_V^p \end{bmatrix} + \begin{bmatrix} \partial \psi_n^{pp} (D_H^p + \delta_p^1) \\ \psi_n^{pp} (D_V^p + \delta_p^1) \end{bmatrix} \right) = \\ & -i\omega\sigma^{(p+1)p} \left( \begin{bmatrix} \xi_n^{pp} B_H^p \\ \partial \xi_n^{pp} B_V^p \end{bmatrix} + \begin{bmatrix} \psi_n^{pp} (D_H^p + \delta_p^1) \\ \partial \psi_n^{pp} (D_V^p + \delta_p^1) \end{bmatrix} \right) \end{aligned} \quad (32)$$

where  $\psi_n^{pq} = j_n(k_p R_q)$ ,  $\xi_n^{pq} = h_n^{(1)}(k_p R_q)$ ,  $\partial \psi_n^{pq} = \frac{1}{\rho} d[\rho j_n(\rho)]|_{\rho=k_p R_q}$ , and  $\partial \xi_n^{pq} = \frac{1}{\rho} d[\rho h_n^{(1)}(\rho)]|_{\rho=k_p R_q}$  ( $d$  is defined as a symbol for the derivative with respect to the radial component). By rearranging the above equations, the coefficients of the layer  $(p + 1)$  can be written in terms of the coefficients of the layer  $p$  as:

$$\begin{bmatrix} B_{H,V}^{(p+1)} \\ D_{H,V}^{(p+1)} \end{bmatrix} = \begin{bmatrix} \frac{1}{T_{Fp}^{H,V}} & \frac{R_{Fp}^{H,V}}{T_{Fp}^{H,V}} \\ \frac{R_{Pp}^{H,V}}{T_{Pp}^{H,V}} & \frac{1}{T_{Pp}^{H,V}} \end{bmatrix} \begin{bmatrix} B_{H,V}^p \\ D_{H,V}^p + \delta_p^1 \end{bmatrix} \quad (33)$$

where the sub/superscripts  $H$  and  $V$  represent the TE and TM waves, respectively. The directions of propagation of these waves are realized through the subscripts  $F$  (outgoing waves) and  $P$  (incoming waves). The effective reflection coefficients are extracted as:

$$R_{Fp}^H = \frac{k_{p+1}\mu_p \partial \psi_n^{(p+1)p} \psi_n^{pp} - k_p \mu_{p+1} \partial \psi_n^{pp} \psi_n^{(p+1)p} + g \psi_n^{pp} \psi_n^{(p+1)p}}{k_{p+1}\mu_p \partial \psi_n^{(p+1)p} \xi_n^{pp} - k_p \mu_{p+1} \partial \xi_n^{pp} \psi_n^{(p+1)p} + g \xi_n^{pp} \psi_n^{(p+1)p}} \quad (34)$$

$$R_{Pp}^H = \frac{k_{p+1}\mu_p \partial \xi_n^{(p+1)p} \xi_n^{pp} - k_p \mu_{p+1} \partial \xi_n^{pp} \xi_n^{(p+1)p} + g \xi_n^{pp} \xi_n^{(p+1)p}}{k_{p+1}\mu_p \partial \xi_n^{(p+1)p} \psi_n^{pp} - k_p \mu_{p+1} \partial \psi_n^{pp} \xi_n^{(p+1)p} + g \psi_n^{pp} \xi_n^{(p+1)p}} \quad (35)$$

$$R_{Fp}^V = \frac{k_{p+1}\mu_p \psi_n^{(p+1)p} \partial \psi_n^{pp} - k_p \mu_{p+1} \psi_n^{pp} \partial \psi_n^{(p+1)p} + g \partial \psi_n^{pp} \partial \psi_n^{(p+1)p}}{k_{p+1}\mu_p \psi_n^{(p+1)p} \partial \xi_n^{pp} - k_p \mu_{p+1} \xi_n^{pp} \partial \psi_n^{(p+1)p} + g \partial \xi_n^{pp} \partial \psi_n^{(p+1)p}} \quad (36)$$

$$R_{Pp}^V = \frac{k_{p+1}\mu_p \xi_n^{(p+1)p} \partial \xi_n^{pp} - k_p \mu_{p+1} \xi_n^{pp} \partial \xi_n^{(p+1)p} + g \partial \xi_n^{pp} \partial \xi_n^{(p+1)p}}{k_{p+1}\mu_p \xi_n^{(p+1)p} \partial \psi_n^{pp} - k_p \mu_{p+1} \psi_n^{pp} \partial \xi_n^{(p+1)p} + g \partial \psi_n^{pp} \partial \xi_n^{(p+1)p}} \quad (37)$$

Moreover, it can be readily shown that the transmission coefficients read as:

$$T_{Fp}^H = \frac{k_{p+1}\mu_p \left( \partial \psi_n^{(p+1)p} \xi_n^{(p+1)p} - \psi_n^{(p+1)p} \partial \xi_n^{(p+1)p} \right)}{k_{p+1}\mu_q \partial \psi_n^{(p+1)p} \xi_n^{pp} - k_p \mu_{p+1} \partial \xi_n^{pp} \psi_n^{(p+1)p} + g \xi_n^{pp} \psi_n^{(p+1)p}} \quad (38)$$

$$T_{Pp}^H = \frac{k_{p+1}\mu_p \left( \partial \xi_n^{(p+1)p} \psi_n^{(p+1)p} - \partial \psi_n^{(p+1)p} \xi_n^{(p+1)p} \right)}{k_{p+1}\mu_p \partial \xi_n^{(p+1)p} \psi_n^{pp} - k_p \mu_{p+1} \partial \psi_n^{pp} \xi_n^{(p+1)p} + g \psi_n^{pp} \xi_n^{(p+1)p}} \quad (39)$$

$$T_{Fp}^V = \frac{k_{p+1}\mu_p \left( \psi_n^{(p+1)p} \partial \xi_n^{(p+1)p} - \xi_n^{(p+1)p} \partial \psi_n^{(p+1)p} \right)}{k_{p+1}\mu_p \psi_n^{(p+1)p} \partial \xi_n^{pp} - k_p \mu_{p+1} \xi_n^{pp} \partial \psi_n^{(p+1)p} + g \partial \xi_n^{pp} \partial \psi_n^{(p+1)p}} \quad (40)$$

$$T_{Pp}^V = \frac{k_{p+1}\mu_p \left( \xi_n^{(p+1)p} \partial \psi_n^{(p+1)p} - \psi_n^{(p+1)p} \partial \xi_n^{(p+1)p} \right)}{k_{p+1}\mu_p \xi_n^{(p+1)p} \partial \psi_n^{pp} - k_p \mu_{p+1} \psi_n^{pp} \partial \xi_n^{(p+1)p} + g \partial \psi_n^{pp} \partial \xi_n^{(p+1)p}} \quad (41)$$

where  $g = i\omega\sigma_{(p+1)p}\mu_p\mu_{p+1}$ . By using  $B_{H,V}^N = D_{H,V}^1 = 0$ , the recurrence relations can be started, and the field expansion coefficients in any desired layer can be obtained. The extinction efficiency is related to the external modified Mie-Lorenz coefficients via:

$$Q_{ext} = \frac{2\pi}{k^2} \Re \sum_{n=1}^{\infty} (2n+1) (B_V^1 + B_H^1) \quad (42)$$

where symbol  $\Re$  represents the real part of the summation. In order to verify the extracted coefficients, the extinction efficiencies of three graphene-coated structures is provided in **Figure 11**. In the graphical representation of the structures, the dashed lines illustrate graphene interfaces, while the solid line shows a PEC core. The optical and geometrical parameters are  $R_1 = 200$  nm,  $R_2 = 100$  nm,  $R_3 = 50$  nm,  $\mu_c = 0.3$  eV,  $T = 300^\circ$  K, and  $\tau = 0.02$  ps. The analytical results are compared with the numerical results of CST 2017 commercial software, and good agreement is achieved. Moreover, the analytical formulation provides a fast and accurate tool for the scattering shaping of various spherical geometries.

In order to realize the priority of the closed-form analytical formulation with respect to the numerical analysis, the simulation times of both methods are included in **Table 2**. Considerable time reduction using the exact solution is evident. Moreover, since 3D meshing and perfectly matched layers are not required in this method, it is efficient in terms of memory as well.

### 3.1.1 Quasistatic approximation and RLC model

Based on the results of Section 3.1, the modified Mie-Lorenz coefficients of the graphene-based spherical particles form infinite summations in terms of spherical Bessel and Hankel functions. In general, graphene plasmons are excited in the sub-wavelength regime, and only the leading order term of the summation is sufficient for achieving the results with acceptable precision. In this regime, the polynomial expansion of the special functions can also be truncated in the first few terms [22]. Later, the extracted modified Mie-Lorenz coefficients can be rewritten in the form of the polynomials. To further simplify the real-time monitoring and performance optimization of the graphene-coated nanoparticles, an equivalent RLC circuit can be proposed by representing the rational functions in the continued fraction form as [36]:

$$Y_{TE/TM} = Y_0 \frac{1}{Z_1 + \frac{1}{Z_2 + \frac{1}{Z_3 + \dots}}} \quad (43)$$

The equivalent circuit corresponding to the above representation is shown in **Figure 12**.



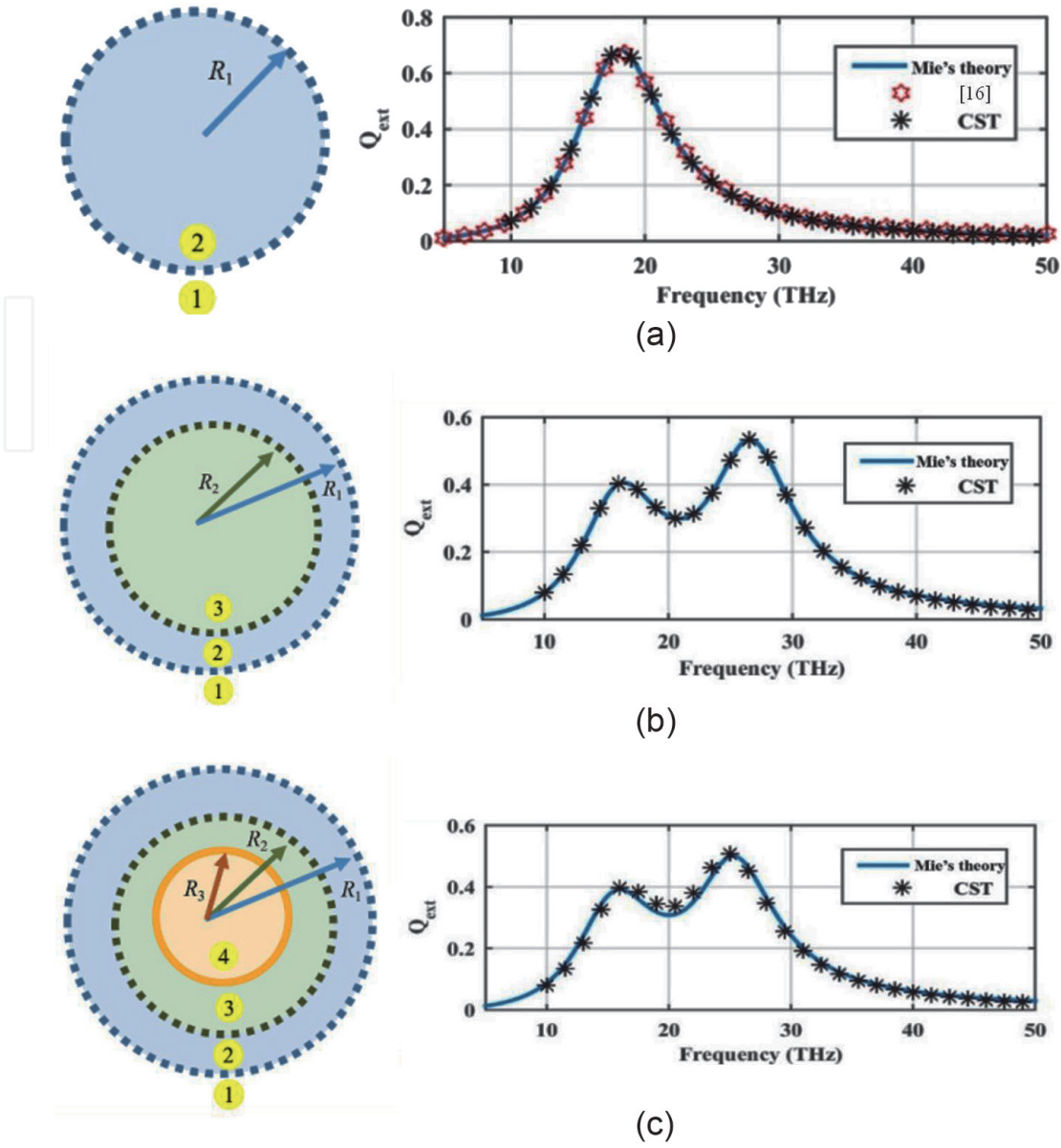


**Figure 11.** The extinction efficiencies of graphene-based particles with different number of layers: (a) two, (b) three, and (c) four [34].

Structure	Simulation time	
	Analytical	CST
Figure 11(a)	0.053214 s	32 h, 50 m, 18 s
Figure 11(b)	0.045831 s	33 h, 45 m, 25 s
Figure 11(c)	0.151555 s	33 h, 34 m, 55 s

**Table 2.** Comparing the simulation time of CST and our codes [34].

The continued fraction representation for the TM coefficients is:

$$b_1 = \frac{x^3}{-\sigma'_2 \sigma'_3{}^{-1} + \frac{x^2}{-\sigma'_1{}^{-1} \sigma'_2{}^{-2} \sigma'_3{}^2 + \frac{x}{\sigma'_1{}^2 \sigma'_2{}^4 \sigma'_3{}^{-4} + O'(x)}}} \quad (44)$$

where  $\sigma'_0 = \sigma'_3{}^{-1} \sigma'_2$ ,  $\sigma'_1 = \sigma'_2{}^{-1} \sigma'_5 - \sigma'_2{}^{-2} \sigma'_3 \sigma'_4$ ,  $\sigma'_2 = i \frac{m}{3} (2 + 2g + m^2)$ ,  $\sigma'_3 = \frac{2m}{9} (-1 + 2g + m^2)$ ,  $\sigma'_4 = \frac{im}{3} \left( -1 + g + \frac{2gm^2}{5} + \frac{9m^2}{10} \right)$ ,  $\sigma'_5 = \frac{4gm}{45} (1 + m^2)$ .

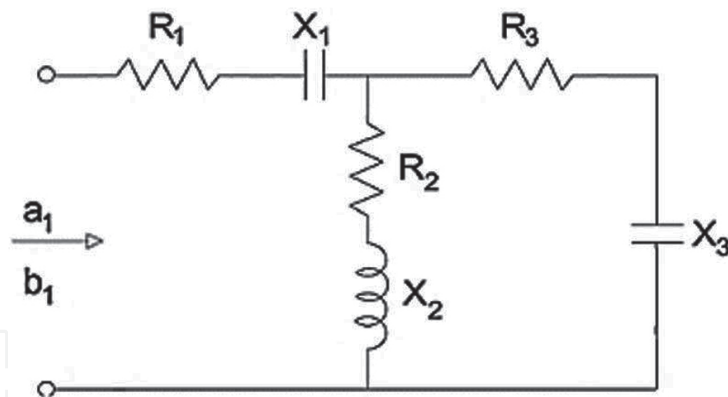


**Figure 12.** The proposed equivalent circuit for the scattering analysis of electrically small graphene-coated spheres [36].

The elements of the equivalent circuit for the TM coefficients read as:

$$Y'_0 = x^3 \quad , \quad Z'_1 = -\sigma'_2 \sigma'_3{}^{-1} \quad , \quad Z'_2 = \frac{-\sigma'_1{}^{-1} \sigma'_2{}^{-2} \sigma'_3{}^2}{x^2} \quad , \quad Z'_3 = x \sigma'_1{}^2 \sigma'_2{}^4 \sigma'_3{}^{-4} \quad (45)$$

### 3.1.2 Application in emission

In order to illustrate the application of Mie analysis for the graphene-wrapped structures, let us consider vertical and horizontal dipoles in the proximity of a graphene-coated sphere, as shown in **Figure 13**. Although in the Mie analysis, the excitation is considered to be a plane wave, by using the scattering coefficients, the total decay rates can be calculated for the dipole emitters, and it can be proven that the localized surface plasmons of the graphene-wrapped spheres can enhance the total decay rate, which is connected to the Purcell factor [16, 37]. The amount of electric field enhancement for the radial-oriented and tangential oscillating dipoles with the distance of  $x_d$ , respectively, read as:

$$\frac{E}{E_0} = 1 + \sum_{n=1}^{\infty} i^{n+1} b_n (2n+1) P_n^1(0) \frac{h_n^{(1)}(x_d)}{x_d} \quad (46)$$

$$\frac{E}{E_0} = 1 + \sum_{n=1}^{\infty} i^n \frac{(2n+1)}{n(n+1)} \left\{ a_n P_n^1(0) h_n^{(1)}(x_d) + i b_n P_n^1(0) \frac{[x_d h_n^{(1)}(x_d)]'}{x_d} \right\} \quad (47)$$

**Figure 13(b)** shows the local field enhancement for the average orientation of the dipole emitter in the vicinity of the sphere with  $R_1 = 20$  nm, coated by a graphene material with the chemical potential of  $\mu_c = 0.1$  eV. As the figure shows, an enhanced electric field in the order of  $\sim 10^4$  is obtained for the dipole distance of 1 nm with averaged orientation, and it decreases as the dipole moves away from the sphere.

### 3.1.3 Application in super-scattering

The possibility of a super-scatterer design using graphene-coated spherical particles is illustrated in **Figure 14**. The design parameters are  $\epsilon_1 = 1.44$ ,  $R_1 = 0.24$   $\mu\text{m}$ , and  $\mu_c = 0.3$  eV. The structure can be simply analyzed by the modified Mie-Lorenz coefficients. The general design concepts are similar to their cylindrical counterparts, namely, dispersion engineering using the associated planar structure, as shown in the inset of the figure. Due to the excitation of TM surface plasmons, the normalized extinction cross-section is five times greater than the bare dielectric

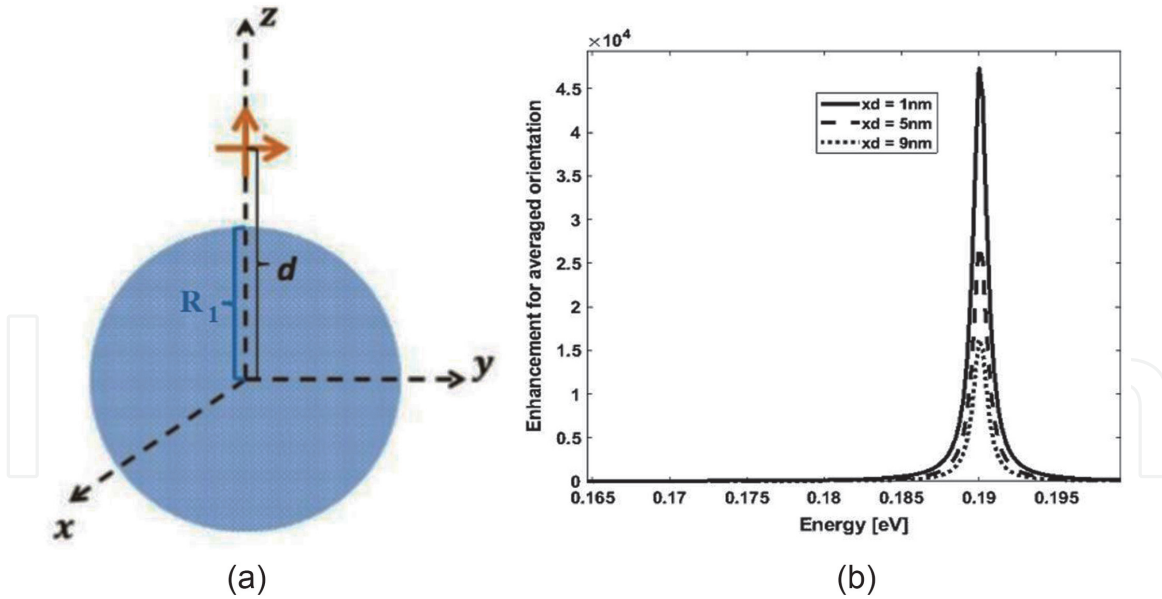


**Figure 13.** (a) Vertical and horizontal dipole emitters in the proximity of the graphene-coated sphere and (b) the local field enhancement for various dipole distances with averaged orientation [37].

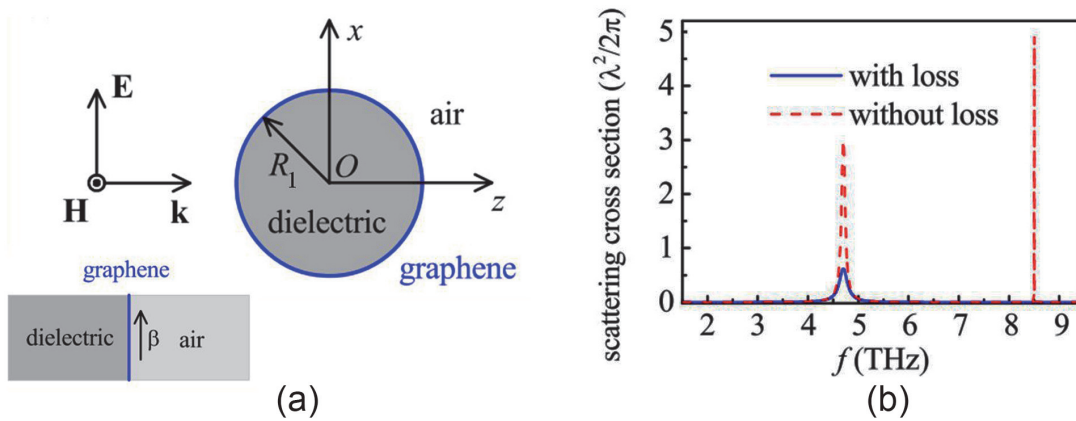


**Figure 14.** (a) Atomically thin super-scatterer and associated planar structure shown in the inset and (b) corresponding normalized scattering cross-sections by considering lossless and lossy graphene shells [38].

sphere. Moreover, similar to the cylindrical super-scatterers, by considering a small amount of loss for the graphene coating by assigning  $\Gamma = 0.11 \text{ meV}$ , the performance is considerably degraded [38].

### 3.1.4 Application in wide-band cloaking

By patterning graphene-based disks with various radii around a dielectric sphere, it is feasible to design a wide-band electromagnetic cloak at infrared frequencies. The geometry of this structure is illustrated in **Figure 15**. In order to analyze the proposed cloak by the modified Mie-Lorenz theory, the polarizability of the disks can be inserted in the equivalent conductivity method. The extracted equivalent surface conductivity can be used to tune the surface reactance of the sphere for the purpose of cloaking [39].

### 3.1.5 Application in multi-frequency cloaking

The other application that can be adapted to our proposed formulation of multilayered spherical structures is multi-frequency cloaking. As **Figure 16** shows, by

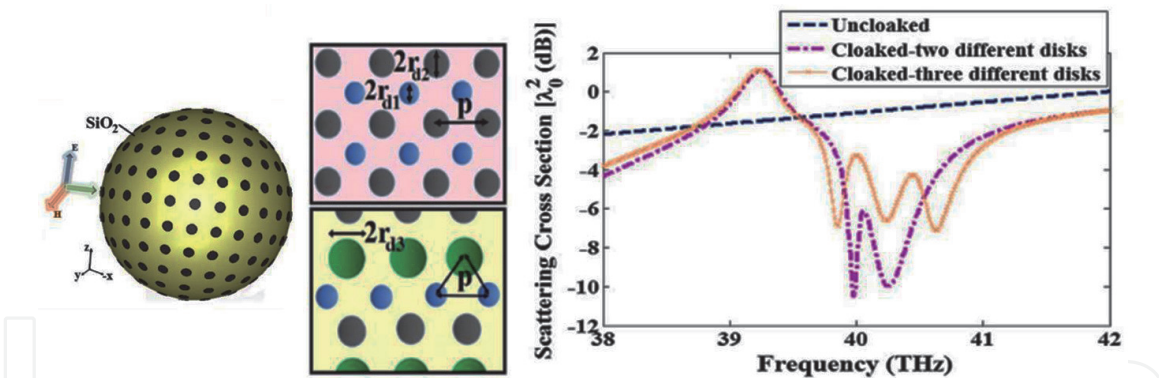


**Figure 15.** Wide-band cloaking using graphene disks with varying radii [39].

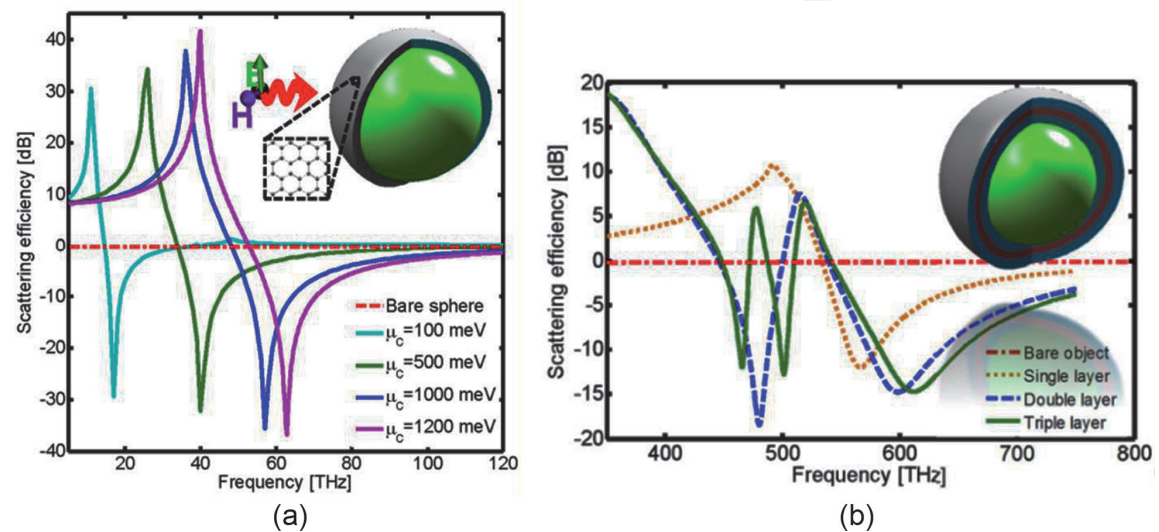


**Figure 16.** (a) Single and (b) multi-frequency cloaking using single/multiple graphene shells around a spherical particle [21].

proper design, a single graphene coating can eliminate the dipole resonance in a single reconfigurable frequency. The radius of the sphere is  $R_1 = 100$  nm and its core permittivity is  $\epsilon_1 = 3$ . It can be concluded that double graphene shells can suppress the scattering in the dual frequencies since each graphene shell with different geometrical and optical properties can support localized surface plasmon resonances in a specific frequency. By further increase of the graphene shells, other frequency bands can be generated. **Figure 16(b)** shows the cloaking performance of a spherical particle with multiple graphene shells. The radii of the spheres are 107.5, 131.5, and 140 nm, and the corresponding chemical potentials are 900, 500, and 700 meV, respectively. The permittivity of the dielectric filler is 2.1 [21].

### 3.1.6 Application in electromagnetic absorption

As another example, a dielectric-metal core-shell spherical resonator (DMCSR) with the resonance frequency lying in the near-infrared spectrum is considered. In order to increase the optical absorption, the outer layer of the structure is covered with graphene. The localized surface plasmons of graphene are mainly excited in the far-infrared frequencies and in the near-infrared and visible range; it behaves like a dielectric. By hybridizing the graphene with a resonator, its optical absorption can be greatly enhanced. **Figure 17** shows the performance of the structure for various core radii [15].

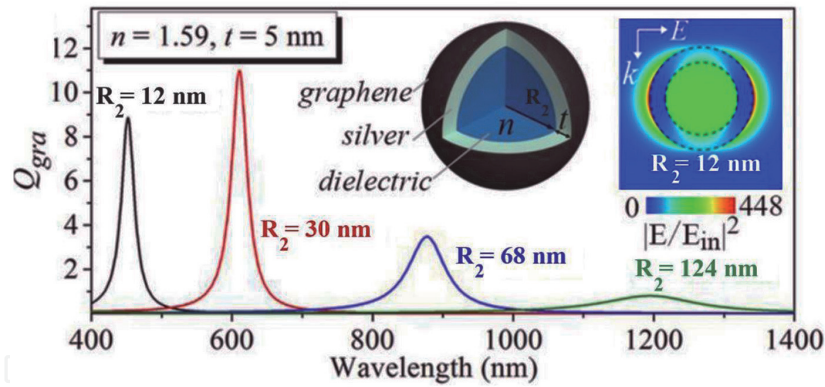


**Figure 17.**

Strong tunable absorption using a graphene-coated spherical resonator with fixed dielectric core refractive index of  $n$  and silver shell thickness of  $t$  [15].

The provided examples are just a few instances for scattering analysis of graphene-based structures. Based on the derived formulas, other novel optoelectronic devices based on graphene plasmons can be proposed. Moreover, since assemblies of polarizable particles fabricated by graphene exhibit interesting properties such as enhanced absorption, negative permittivity, giant near-field enhancement, and large enhancements in the emission and the radiation of the dipole emitters [40–43], the research can be extended to the multiple scattering theory.

## Author details


Shiva Hayati Raad<sup>1</sup>, Zahra Atlasbaf<sup>1\*</sup> and Mauro Cuevas<sup>2</sup>

<sup>1</sup> Department of Electrical and Computer Engineering, Tarbiat Modares University, Tehran, Iran

<sup>2</sup> Faculty of Engineering and Information Technology, University of Belgrano, Buenos Aires, Argentina

\*Address all correspondence to: atlasbaf@modares.ac.ir

## IntechOpen

© 2020 The Author(s). Licensee IntechOpen. This chapter is distributed under the terms of the Creative Commons Attribution License (<http://creativecommons.org/licenses/by/3.0>), which permits unrestricted use, distribution, and reproduction in any medium, provided the original work is properly cited. 

## References

- [1] Kim K-H, No Y-S. Subwavelength core/shell cylindrical nanostructures for novel plasmonic and metamaterial devices. *Nano Convergence*. 2017;**4**(1):1-13
- [2] Fan P, Chettiar UK, Cao L, Afshinmanesh F, Engheta N, Brongersma ML. An invisible metal–semiconductor photodetector. *Nature Photonics*. 2012;**6**(6):380
- [3] Padooru YR, Yakovlev AB, Chen P-Y, Alù A. Analytical modeling of conformal mantle cloaks for cylindrical objects using sub-wavelength printed and slotted arrays. *Journal of Applied Physics*. 2012;**112**(3):034907
- [4] Ruan Z, Fan S. Superscattering of light from subwavelength nanostructures. *Physical Review Letters*. 2010;**105**(1):013901
- [5] Qian C et al. Experimental observation of superscattering. *Physical Review Letters*. 2019;**122**(6):063901
- [6] Naserpour M, Zapata-Rodríguez CJ. Tunable scattering cancellation of light using anisotropic cylindrical cavities. *Plasmonics*. 2017;**12**(3):675-683
- [7] Díaz-Aviñó C, Naserpour M, Zapata-Rodríguez CJ. Conditions for achieving invisibility of hyperbolic multilayered nanotubes. *Optics Communications*. 2016;**381**:234-239
- [8] Garcia-Etxarri A et al. Strong magnetic response of submicron silicon particles in the infrared. *Optics Express*. 2011;**19**(6):4815-4826
- [9] Monticone F, Argyropoulos C, Alù A. Layered plasmonic cloaks to tailor the optical scattering at the nanoscale. *Scientific Reports*. 2012;**2**:912
- [10] Liu W, Lei B, Shi J, Hu H. Unidirectional superscattering by multilayered cavities of effective radial anisotropy. *Scientific Reports*. 2016;**6**:34775
- [11] Velichko EA. Evaluation of a graphene-covered dielectric microtube as a refractive-index sensor in the terahertz range. *Journal of Optics*. 2016;**18**(3):035008
- [12] Correas-Serrano D, Gomez-Diaz JS, Alù A, Melcón AÁ. Electrically and magnetically biased graphene-based cylindrical waveguides: Analysis and applications as reconfigurable antennas. *IEEE Transactions on Terahertz Science and Technology*. 2015;**5**(6):951-960
- [13] Li R et al. Design of ultracompact graphene-based superscatterers. *IEEE Journal of Selected Topics in Quantum Electronics*. 2016;**23**(1):130-137
- [14] Bernety HM, Yakovlev AB. Cloaking of single and multiple elliptical cylinders and strips with confocal elliptical nanostructured graphene metasurface. *Journal of Physics: Condensed Matter*. 2015;**27**(18):185304
- [15] Wan M et al. Strong tunable absorption enhancement in graphene using dielectric-metal core-shell resonators. *Scientific Reports*. 2017;**7**(1):32
- [16] Christensen T, Jauho A-P, Wubs M, Mortensen NA. Localized plasmons in graphene-coated nanospheres. *Physical Review B*. 2015;**91**(12):125414
- [17] Xiao T-H, Gan L, Li Z-Y. Graphene surface plasmon polaritons transport on curved substrates. *Photonics Research*. 2015;**3**(6):300-307
- [18] Falkovsky LA. Optical properties of graphene and IV–VI semiconductors. *Physics-Uspekhi*. 2008;**51**, 9:887
- [19] Hanson GW. Dyadic Green's functions and guided surface waves for

a surface conductivity model of graphene. *Journal of Applied Physics*. 2008;**103**(6):064302

[20] Vakil A. Transformation Optics Using Graphene: One-Atom-Thick Optical Devices Based on Graphene. Dissertations-University of Pennsylvania; 2012

[21] Farhat M, Rockstuhl C, Bağcı H. A 3D tunable and multi-frequency graphene plasmonic cloak. *Optics Express*. 2013;**21**(10):12592-12603

[22] Bohren CF, Huffman DR. Absorption and Scattering of Light by Small Particles. New York: John Wiley & Sons; 2008

[23] Naserpour M, Zapata-Rodríguez CJ, Vuković SM, Pashaeiadi H, Belić MR. Tunable invisibility cloaking by using isolated graphene-coated nanowires and dimers. *Scientific Reports*. 2017;**7**(1): 12186

[24] Riso M, Cuevas M, Depine RA. Tunable plasmonic enhancement of light scattering and absorption in graphene-coated subwavelength wires. *Journal of Optics*. 2015;**17**(7):075001

[25] Pashaeiadi H, Naserpour M, Zapata-Rodríguez CJ. Scattering of electromagnetic waves by a graphene-coated thin cylinder of left-handed metamaterial. *Optik*. 2018;**159**:123-132

[26] Cuevas M, Riso MA, Depine RA. Complex frequencies and field distributions of localized surface plasmon modes in graphene-coated subwavelength wires. *Journal of Quantitative Spectroscopy and Radiative Transfer*. 2016;**173**:26-33

[27] Abramowitz M, Stegun IA, editors. *Handbook of Mathematical Functions with Formulas, Graphs, and Mathematical Tables*. Vol. 55. US Government Printing Office; 1948

[28] Cuevas M. Graphene coated subwavelength wires: A theoretical investigation of emission and radiation properties. *Journal of Quantitative Spectroscopy and Radiative Transfer*. 2017;**200**:190-197

[29] Cuevas M. Enhancement, suppression of the emission and the energy transfer by using a graphene subwavelength wire. *Journal of Quantitative Spectroscopy and Radiative Transfer*. 2018;**214**:8-17

[30] Raad SH, Zapata-Rodríguez CJ, Atlasbaf Z. Multi-frequency super-scattering from sub-wavelength graphene-coated nanotubes. *JOSA B*. 2019;**36**(8):2292-2298

[31] Díaz-Aviñó C, Naserpour M, Zapata-Rodríguez CJ. Optimization of multilayered nanotubes for maximal scattering cancellation. *Optics Express*. 2016;**24**(16):18184-18196

[32] Chen P-Y, Soric J, Padooru YR, Bernety HM, Yakovlev AB, Alù A. Nanostructured graphene metasurface for tunable terahertz cloaking. *New Journal of Physics*. 2013;**15**(12):123029

[33] Raad SH, Zapata-Rodríguez CJ, Atlasbaf Z. Graphene-coated resonators with frequency-selective super-scattering and super-cloaking. *Journal of Physics D: Applied Physics*. 2019;**52**(49):495101

[34] Raad SH, Atlasbaf Z, Rashed-Mohassel J, Shahabadi M. Scattering from Graphene-based multilayered spherical structures. *IEEE Transactions on Nanotechnology*. 2019;**18**:1129-1136

[35] Li L-W, Kooi P-S, Leong M-S, Yee T-S. Electromagnetic dyadic Green's function in spherically multilayered media. *IEEE Transactions on Microwave Theory and Techniques*. 1994;**42**(12):2302-2310

[36] Raad SH, Atlasbaf Z. Equivalent RLC ladder circuit for scattering by graphene-coated nanospheres. *IEEE Transactions on Nanotechnology*. 2019; **18**:212-219

[37] Sijercic E, Leung P. Enhanced terahertz emission from quantum dot by graphene-coated nanoparticle. *Applied Physics B*. 2018;**124**(7):141

[38] Li R, Lin X, Lin S, Liu X, Chen H. Atomically thin spherical shell-shaped superscatterers based on a Bohr model. *Nanotechnology*. 2015;**26**(50):505201

[39] Shokati E, Granpayeh N, Danaeifar M. Wideband and multi-frequency infrared cloaking of spherical objects by using the graphene-based metasurface. *Applied Optics*. 2017; **56**(11):3053-3058

[40] Raad SH, Atlasbaf Z. Tunable optical absorption using Graphene covered Core-Shell Nano-spheres. In: *Iranian Conference on Electrical Engineering (ICEE)*. IEEE; 2018. pp. 98-102

[41] Raad SH, Atlasbaf Z. Tunable optical meta-surface using graphene-coated spherical nanoparticles. *AIP Advances*. 2019;**9**(7):075224

[42] Raad SH, Atlasbaf Z, Zapata-Rodríguez CJ. Multi-frequency near-field enhancement with graphene-coated nano-disk homo-dimers. *Optics Express*. 2019;**27**(25):37012-37024

[43] Cuevas M. Theoretical investigation of the spontaneous emission on graphene plasmonic antenna in THz regime. *Superlattices and Microstructures*. 2018;**122**:216-227